MATERIALS CHEMISTRY FRONTIERS

CHINESE CHEMICAL SOCIETY

ROYAL SOCIETY OF CHEMISTRY

RESEARCH ARTICLE

View Article Online
View Journal

Cite this: DOI: 10.1039/d2qm00088a

Structure–property relationship on insertion of fluorine- *versus* nitrogen substituents in wide bandgap polymer donors for non-fullerene solar cells: an interesting case study†

Gururaj P. Kini, Yong Woon Han, Sung Jae Jeon, Yoon Jae Lee and Doo Kyung Moon *

Received 4th February 2022,
Accepted 11th April 2022

DOI: 10.1039/d2qm00088a

rsc.li/frontiers-materials

In organic solar cell research, developing efficient and low-cost photovoltaic materials *via* insertion of fluorine (F) and nitrogen (N) substituents has proved as a highly successful strategy, thus raising the question of choosing between these substituents while designing new materials. In this work, two new low-cost polymer donors, **P1-2F** and **P2-2N**, based on an alternate chlorinated thienyl benzodithiophene donor and 2,5-difluorobenzene (2FBn) and pyrazine (Pz) as a unit as the acceptor core, respectively, were synthesized and compared in parallel to investigate the synergistic effects of the insertion of F and N substituents (functional group *vs.* atomic substitution) on the morphology and photovoltaic performance. Although both strategies effectively lower the frontier molecular orbital (FMO) energy levels because of the high electronegativity of these substituents, favorable positioning of the N atom in Pz led to further improved coplanarity, a lower bandgap of 2.07 eV, and enhanced crystallinity and molecular ordering with a shorter π–π spacing distance in **P2-2N** as revealed by density functional theory and X-ray diffraction results. Besides, combining with the 3,9-bis(2-methylene-((3-(1,1-dicyanomethylene)-6,7-difluoro)-indanone))-5,5,11,11-tetrakis(4-hexylphenyl)-dithieno[2,3-*d*:2′,3′-*d*′]-s-indaceno[1,2-*b*:5,6-*b*′]dithiophene (**IT-4F**) acceptor, **P2-2N** also maintained optimal nanoscale morphology, excellent charge transfer, and high and more balanced hole and electron mobilities, which subsequently resulted in a remarkable power conversion efficiency of 9.5% with a low energy loss (E_{loss}) of 0.61 eV and outperformed the corresponding F counterpart **P1-2F** (8.1% and E_{loss} of 0.65 eV). The in-depth study using various characterization tools suggested that the lower performance of **P1-2F** resulted from the inferior nanoscale morphology caused by poor mixing with **IT-4F**, which significantly reduced the charge carrier mobility and efficient charge transfer. Consequently, these results provide deeper insights and mechanisms for further designing efficient donors with either F or N substituents.

1. Introduction

Over the years, organic solar cells (OSCs) have successfully evolved as the most reliable among futuristic renewable energy technologies because of their distinctive benefits such as solution processability, light weight, semitransparency, low-cost and large-scale roll-to-roll fabrication, *etc.*, and it is believed that they will enter the commercial market soon.[1–7] Recently, swift developments in the rational design of low bandgap (LBG) non-fullerene small molecule acceptors (NFAs) with excellent extinction coefficients and high electron mobilities (μ_e) have been witnessed,[8–12] which rapidly enhanced the power conversion efficiency (PCE) of organic solar cells (OSCs) from 10% to 18%.[8,9,11,13–21] Despite this impressive performance, the relatively low open-circuit voltage (V_{oc}) due to the LBG of NFAs and the high synthesis cost of the donor and acceptor materials are the hurdles for commercializing OSCs.[22–25] Henceforth, developing novel wide bandgap (WBG) donors having deep highest occupied molecular orbital (HOMO) levels and superior matching with current efficient NFAs and reducing the overall cost of both donor and acceptor by employing simple structured molecular design is gaining significant attention among the OSC research communities. Many studies have been reported recently in this direction.[15,23,26,27]

Nano and Information Materials (NIMs) Laboratory, Department of Chemical Engineering, Konkuk University, 120, Neungdong-ro, Gwangjin-gu, Seoul 05029, Korea. E-mail: dkmoon@konkuk.ac.kr; Fax: +82-2-444-0765; Tel: +82-2-450-3498

† Electronic supplementary information (ESI) available: Experimental section, detailed synthesis of intermediates (^{1}H and ^{13}C NMR), polymers and additional figures and tables as mentioned in the main text. See DOI: https://doi.org/10.1039/d2qm00088a

Among the commercially viable designs to develop low-cost photoactive materials, insertion of intramolecular "noncovalent interactions/locks" (NCLs) like S···O, S···N, S···F and F···H within the aromatic backbones has become a reliable method over the years.[28–30] In addition to advantages such as enhanced rigidity, coplanarity, and improved charge transport in the semiconducting backbone, these NCLs also proved to aid significantly in reducing the overall cost by minimizing tedious synthetic steps.[26,28,29,31–35] Therefore, a variety of new donors and NFAs have been synthesized, employing this strategy.[7,26,28,29,31–37] Although all types of NCLs can effectively enhance the coplanarity of the conjugated backbone by decreasing the steric repulsion between the neighboring molecules, the introduction of N···S and F···S NCLs further reduce the HOMO energy levels due to the higher electronegativity of N and F substituents.[28,38] Thus, both these modifications remain the preferred choice for designing photovoltaic materials with deep HOMO energy levels, which recently delivered a remarkable performance in the corresponding OSCs.[23,26,32,39,40] Besides, it is essential to note that most of these reports emphasize the effect of the intrinsic properties of either F or N substituents, including the extent, substitution position, and comparative study with a similar class of materials.[29,39,41–44] However, there is no direct comparative structure–property relationship study to emphasize how differently F···S and N···S NCLs will affect the polymer conformation, molecular packing and crystallinity, nanoscale morphology and photovoltaic properties despite both having different functionalization patterns (*i.e.*, fluorination is functional group variation, whereas N-insertion is heteroatom substitution). The recent impressive results incorporating these unique strategies will raise the question of how to select between insertion of F and N substituents while designing a new efficient donor or acceptor unit for OSC applications.

As both these strategies are already matured, we first compare the intrinsic properties of these substituents to gain a deeper understanding of their effects. (1) Electronegativity: even though both these substituents have proved their potential for decreasing both the HOMO and lowest unoccupied molecular orbital (LUMO) energy levels, the higher electronegativity of F compared to N (Pauling electronegativity = 4.0 and 3.04 eV, respectively, for F and N atoms)[45,46] will further deepen the molecular energy level of the conjugated molecule. Additionally, this high electronegativity character will promote intermolecular or intramolecular noncovalent interactions, resulting in higher backbone planarity. (2) Dipole moment: unlike the –C–F bond (which has a fixed dipole moment (μ) of 1.41 D),[47] the μ of the C–N bond can be significantly varied due to the versatility of the N atom having five valence electrons, which can form stable –C–N single bonds (as in amines or amides) and –C=N double bonds (like in imines and pyridines) and –C≡N (as in nitrile).[48] Hence, as reported by Hou *et al.*,[49] we performed the computational calculations of basic aromatic benzene derivatives, *i.e.*, fluorobenzene, pyridine, 1,2-difluorobenzene, and pyridazine units, using density functional theory to predict the effect of the F and N substituents on μ as shown in Fig. S5 (ESI†). Interestingly, the replacement of F by N atoms resulted in enhanced μ and thus can facilitate red-shifted absorption and self-assembly due to the stronger intramolecular charge transfer (ICT) effect. (3) The van der Waals radii: both these atoms exhibit smaller van der Waals radii (1.70 and 1.60 Å for N and F atoms, respectively),[50] thereby causing enhanced planarity in the conjugated molecule without a severe steric effect. However, attributed to the different nature and substitution positions of –C–F (F atom lies outside the benzene ring) and –C=N bonds (N atom will be in conjugation with a benzene ring), their effects on molecular geometry were elucidated by DFT calculations on dithienyl-substituted benzene, fluorobenzene and pyridine as shown in Fig. S6 (ESI†). Notably, the parent unsubstituted benzene core has a torsion angle of $>25^{\circ}$ between benzene and adjacent thiophene. Interestingly, the dihedral angle between fluorobenzene and pyridine and adjacent thiophene drastically lowered to $\sim 11.93^{\circ}$ and 0.15° after the addition of fluorine and nitrogen, respectively, due to the N···S and F···S NCLs, respectively. These results clearly demonstrate that N-containing aromatic compounds have a relatively higher planarity than the F-substituted counterparts because N atom is in conjugation with the benzene ring in Pz units. Overall, these small changes can significantly alter the molecular packing and charge transport in related compounds.

Thus, to provide direct comparison effects of F···S and N···S NCLs through F and N insertion on the properties and photovoltaic performance of polymer donors, we designed two WBG polymer donors, poly-{4,8-bis(4-chloro-5-(2-ethylhexyl)thiophen-2-yl)-2-(3-(2-ethylhexyl)-5-(4-(4-(2-ethylhexyl)-5-methylthiophen-2-yl)-2,5-difluorophenyl)thiophen-2-yl)-6-methylbenzo[1,2-*b*:4,5-*b*′]dithiophene} (**P1-2F**) and poly-{2-(5-(4,8-bis(4-chloro-5-(2-ethylhexyl)thiophen-2-yl)-6-methylbenzo[1,2-*b*:4,5-*b*′]dithiophen-2-yl)-4-(2-ethylhexyl)thiophen-2-yl)-5-(4-(2-ethylhexyl)-5-methylthiophen-2-yl)pyrazine}(**P2-2N**), having the same chlorinated-thienyl benzodithiophene (Cl-BDT)

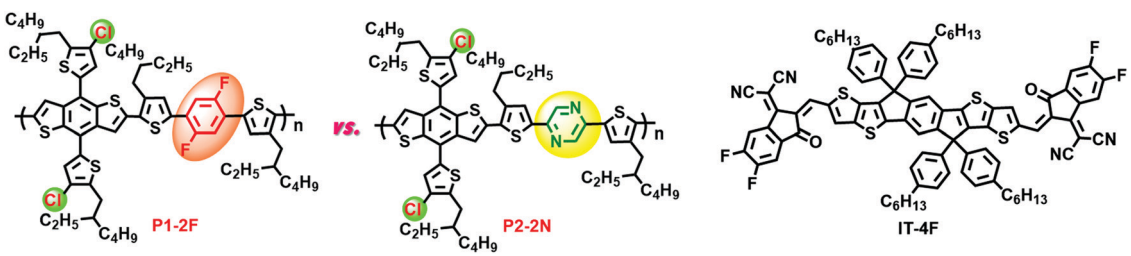

Scheme 1 Chemical structures of the **P1-2F** and **P2-2N** donor polymers and **IT-4F** acceptor used in this study.

donor and 2,5-difluorobenzene (2FBn) and pyrazine (Pz) as a unit as the acceptor core, respectively (Scheme 1). Among the available low-cost benzene derivatives, 2FBn and Pz units were chosen in the following study due to their commercial availability at a low price, therefore minimizing the overall synthetic complexity. Moreover, both have "C2 symmetry" with symmetrically placed F or N substituents aiding planarization of the backbone *via* NCLs and an aromatic benzene ring with a large WBG together with F and N-substituents having high electronegativity and thus helping to lower the HOMO and V_{oc} in the corresponding devices paired with appropriately matching LBG NFAs. Here, we found that **P2-2N** displays red-shifted absorption, enhanced crystallinity, and favorable molecular ordering with a shorter π–π spacing compared to **P1-2F** and a superior nanoscale morphology to **P2-2N**:**IT-4F**-based blend films. Thus, **P2-2N**-based devices showed a remarkable PCE of 9.5%, with an overall improvement in all the photovoltaic parameters. On the other hand, **P1-2F** realizes a moderate photovoltaic performance of 8.1% due to a lower charge mobility, poor exciton harvesting and inferior phase-separated morphology with a large domain size. Thus, with the aid of diverse characterization techniques, a clear structure–property relationship study to reveal the distinct effect of N···S and F···S NCLs on energy level modulation, coplanarity, molecular ordering, morphology, and device performance was performed. Last, this is one of the impressive values among the low-cost polymer design involving alternate BDT and thiophene and/or heteroarene units with various electron-withdrawing substituents as a weak "A" unit reported in the literature (Fig. S7, ESI†).

2. Results and discussion

The synthetic routes of monomers and polymers are given in Fig. 1 and relevant characterization along with a detailed synthetic process is provided in the ESI.† The monomers **2FBn-Br** and **Pz-Br** were synthesized from the commercially available cheap starting materials 1,4-dibromo-2,5-difluorobenzene (1) and 2,5-dibromopyrazine (2) in two simple steps as reported in a previous report.[35,40] Then, copolymers **P1-2F**

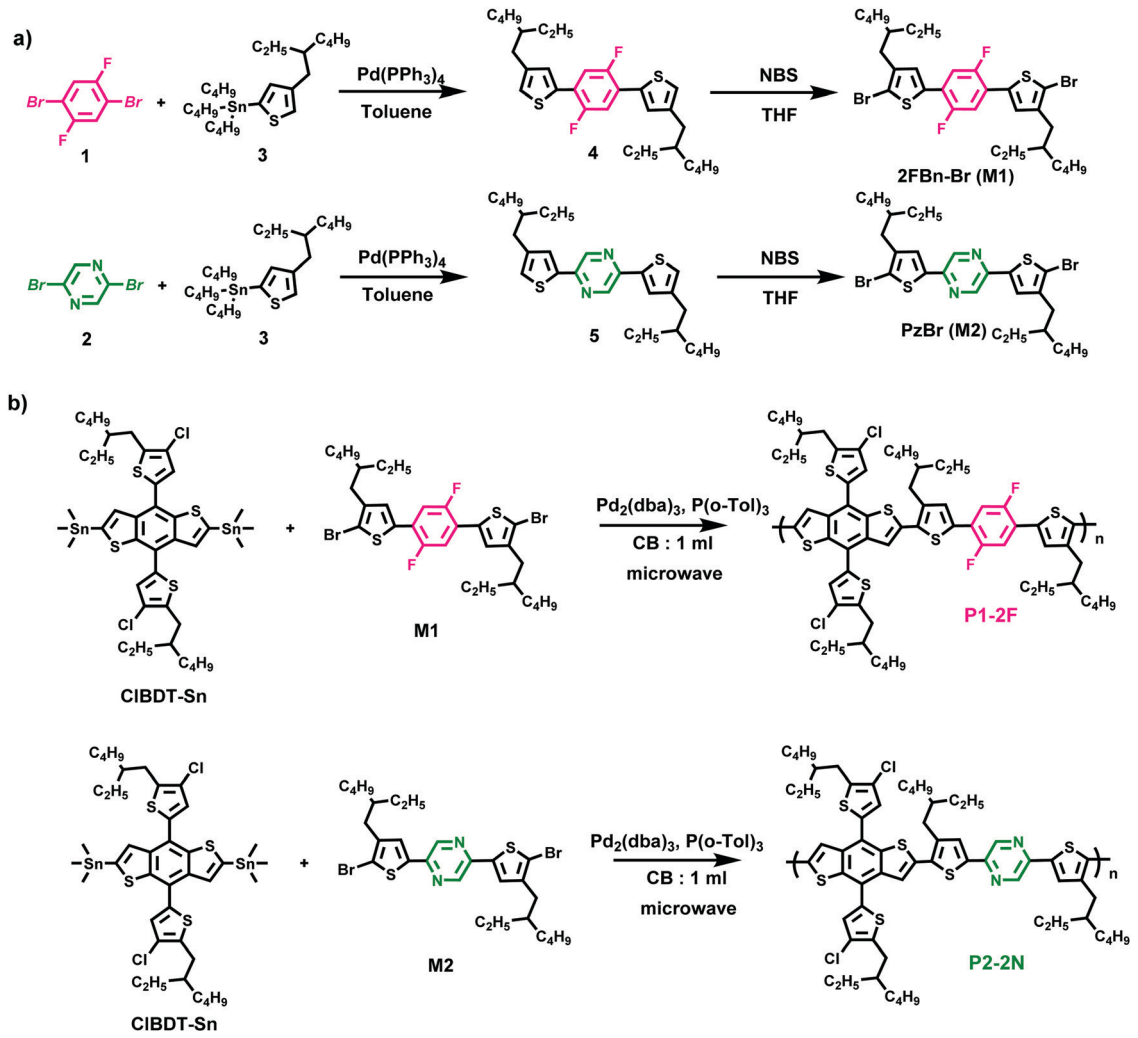

Fig. 1 Synthetic routes of (a) monomers M1 and M2 and (b) polymers **P1-2F** and **P2-2N**.

and **P2-2N** were prepared by Stille copolymerization of ClBDT-Sn with **2FBn-Br** or **Pz-Br**, respectively, under a microwave reactor using chlorobenzene (CB) as a solvent. Both the copolymers have good solubility in chloroform and CB. The number-average molecular weights (M_n) of **P1-2F** and **P2-2N** were 32.2 and 30.4 kDa, respectively, with corresponding dispersity ($Đ$) values of 3.4 and 3.1. As shown in Fig. S8 (ESI†), the thermal properties of the polymers were estimated using thermogravimetric analysis (TGA). **P1-2F** and **P2-2N** displayed thermal decomposition temperatures of 431 °C and 421 °C, respectively, at a 5% weight loss, adequate for OSC applications.

Density functional theory (DFT) calculations at the B3LYP/6-31G* level were performed to understand the distinct effects of F or N substitution molecular geometries and frontier molecular orbitals of the two polymers. To minimize the complexity and save time, 2-ethylhexyl chains in the original polymer structure were modified to methyl chains, and calculations based on two repeating units of polymers were performed, as shown in Fig. 2. Furthermore, computational calculations based on the benzene-based polymer (P-Bn) structure were also included to understand the existence of noncovalent interactions due to the insertion of F and N substituents in newly synthesized polymers (Fig. S9, ESI†). In the case of P-Bn, the dihedral angle between the thiophene adjacent to benzene is found to be θ_2 = 23.59° and θ_2 = 23.16°, which is significantly larger than for 2FBn (θ_2 = 3.51° and θ_3 = 9.81°) and pyrazine (θ_2 = 0.36° and θ_3 = 1.97°). Additionally, they also showed a larger angle between Cl-BDT and the thiophene counterpart (θ_1/θ_4 = 30.78°/32.28°, 30.28°/30.53° and 28.34°/25.39° for P-Bn, **P1-2F** and **P2-2N**, respectively). These results substantiate the existence of noncovalent F···S and F···H NCL interactions between the F substituents of the 2FBn in **P1-2F**, and N···S and N···H interactions between the nitrogen atoms of the pyrazine in **P2-2N**, which can improve the molecular planarity, molecular packing, and charge transfer as reported previously.[26,35,40,51] Interestingly, among the polymers, **P2-2N** not only showed the lowest dihedral angle along the backbone but also exhibited a shorter C–C bond length between Pz and its adjacent thiophene (145.33 pm) compared to **P1-2F** (145.98 pm) (Fig. 2(a)). These trends provide clear evidence that the introduction of Pz (since N is in conjugation with a benzene ring) further promotes greater planarization of the backbone and eventually leads to a lower bandgap in **P2-2N** by minimizing rotation barriers compared to **P1-2F** (where F lies outside the benzene ring in 2FBn, which causes minor torsion). Besides, as shown in Fig. 2(b) and (c), HOMO and LUMO electron clouds were equally distributed along the complete polymer backbone, suggesting effective delocalization of π-electrons *via* a strong ICT effect (Fig. 2(b) and (c)). Also, the corresponding $HOMO_{DFT}$ and $LUMO_{DFT}$ energy levels were calculated to be −5.05 and −2.45 eV for **P1-2F** and −5.01 and −2.30 eV for **P2-2N**, respectively. These trends in FMO energy levels agreed with the experimental results (discussed below) and deeper HOMO/LUMO energy levels of **P1-2F** attributed to the more substantial electron-withdrawing effect of F over N. Lastly, the electrostatic surface potential (ESP) reveals that both polymers had a continuous negative potential along the polymer backbone, whereas electron-withdrawing F and N atoms showed positive ESPs (Fig. 2(d)).

The ultraviolet-visible (UV-vis) absorption spectra of the copolymers in solution and thin film states are shown in Fig. 3(a) and (b). The corresponding optical parameters are summarized in Table 1. In chloroform (CF) solution, **P1-2F** displayed an intense absorption band ranging from 450 to 550 nm with a maximum molar absorptivity coefficient (ε_{max}) of 7.18 × 10^4 M^{-1} cm^{-1} centered around 492 nm. In comparison, **P2-2N** displayed relatively ∼30 nm red-shifted absorption profiles along with a relatively low ε_{max} of 6.39 × 10^4 M^{-1} cm^{-1} at 525 nm. Meanwhile, in the film state, although both polymers exhibit similar absorption trends as in the solutions, they showed much broader and bathochromically shifted (∼50 nm) spectra, which is indicative of the strong intermolecular π–π stacking.[52–54] The optical energy gaps of **P1-2F** and **P2-2N** were estimated to be 2.17 eV and 2.07 eV, respectively, calculated from the corresponding absorption onsets (λ_{onset}) located at 575 and 603 nm. Further, we measured the absorptivity coefficients of these new polymers in the film state. The absorption

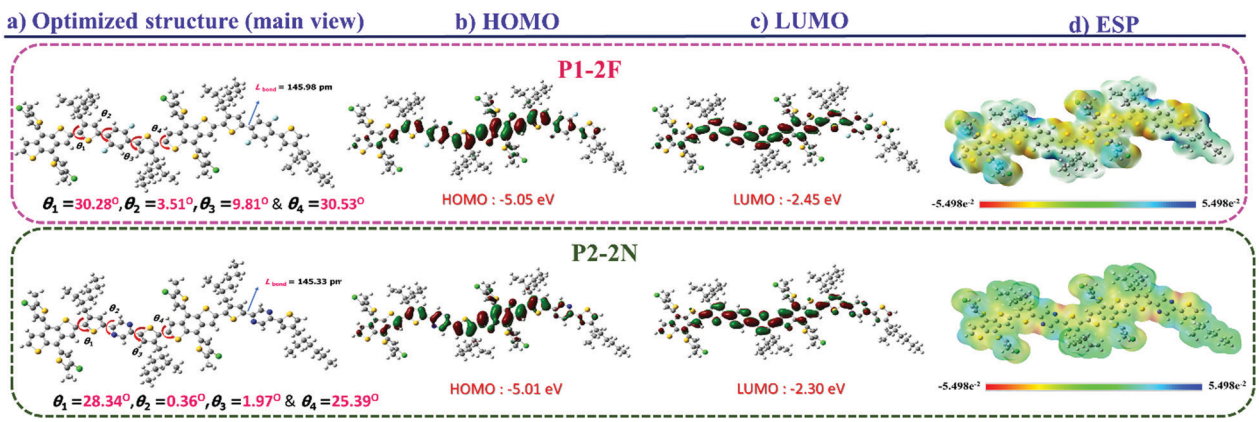

Fig. 2 (a) Optimized geometries and (b) HOMO and (c) LUMO energy levels and maps of the electrostatic potential (ESP) surfaces of the dimer model molecules of the **P1-2F** and **P2-2N** polymers (calculated using the Gaussian 09 package at the B3LYP/6-31G level).

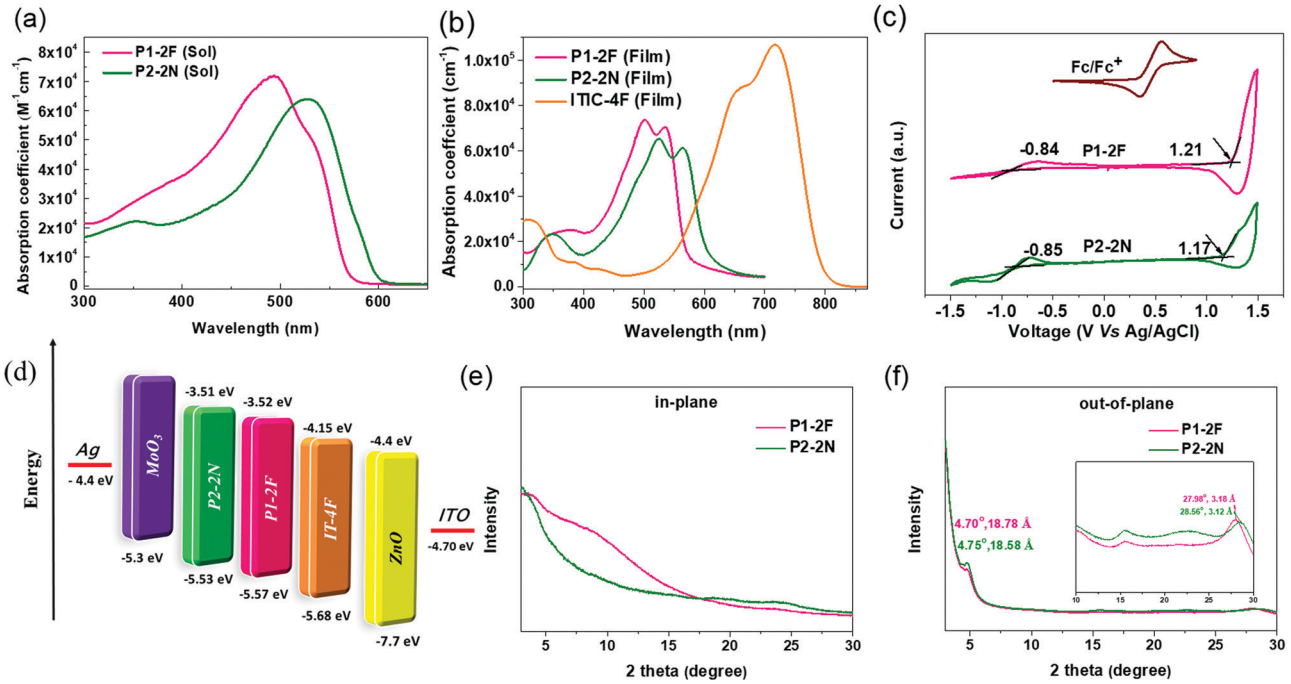

Fig. 3 Absorption spectra of the polymers in (a) CF solutions and (b) the thin-film state, (c) corresponding cyclic voltammograms, (d) energy level alignment of polymers and other components in the OSCs, and (e) in-plane (q_{xy}) and (f) out-of-plane (q_z) line cut profiles of the pristine **P1-2F** and **P2-2N** polymers obtained from XRD.

Table 1 Summary of the optical and electrochemical properties of the newly synthesized polymers

		Thermal property	Optical properties				Electrochemical properties		
Polymer	M_n [kDa]/$Đ^a$	T_d [°C]^b	λ_{max} [nm], solution	λ_{max} [nm], thin film	λ_{onset} [nm], thin film	E_g^{opt} [eV]^c	HOMO [eV]^d	LUMO [eV]^d	E_g^{elect} [eV]^e
P1-2F	32.2/3.4	431	492	500, 535	575	2.17	−5.57	−3.52	2.05
P2-2N	30.4/3.1	421	525	525, 562	603	2.07	−5.53	−3.51	2.02

^{a} Measured by GPC. ^{b} Decomposition temperature (T_d, with a 5% weight loss) was calculated by TGA. ^{c} Estimated values from the UV-vis absorption edge of the thin film (E_g^{opt} = 1240/λ_{onset}, eV). ^{d} $E_{HOMO\ (or\ LUMO)}$ = −[E_{onset} (*vs.* Ag/AgCl) − $E_{1/2}$ of Fc/Fc$^+$ (*vs.* Ag/AgCl)] − 4.8 [eV] (measured $E_{1/2}$ of Fc/Fc$^+$ (*vs.* Ag/AgCl) = 0.44 eV). ^{e} Electrochemical bandgap estimated from the difference between onset oxidation and reduction potentials of the polymers.

coefficients of **P1-2F** and **P2-2N** (at 520 nm) and **IT-4F** (at 715 nm) films were 7.38, 6.52 × 10^4 M^{-1} cm^{-1} and 10.68 × 10^5 M^{-1} cm^{-1}, respectively. Although **P1-2F** demonstrated a higher absorptivity coefficient than the **P2-2N** counterpart in both film and solution states, the red-shifted and well-complementary absorption of **P2-2N** with the **IT-4F** acceptor is expected to produce effective light-harvesting of the solar spectrum by covering the valley region around 575 nm. These results demonstrate that a minor modification in the polymer backbone *via* substituent variation or heteroatom insertion caused a substantial effect on their ε_{max} values and the intermolecular interactions and molecular packing in the solid state. These results agree well with the DFT trends.

Cyclic voltammetry was used to study the effect of insertion of F and N atoms on the frontier energy levels of the copolymers. The HOMO and LUMO energy levels of the polymers in the thin film state were estimated from their corresponding offset oxidation and reduction potentials against the Fc/Fc$^+$ standard (Fig. 3(c)). From the CV profile in Fig. 3(c), the calculated HOMO/LUMO energy levels of **P1-2F** and **P2-2N** are −5.57/−3.52 eV and −5.53/−3.51 eV, which lead to the electrochemical bandgaps of 2.05 and 2.02 eV, respectively, deduced from the onset potential of oxidation and reduction. Notably, there is a small variation in the optical and electrochemical bandgap values of the polymers, which is attributed to the interface barrier between the polymer film and electrode surface. The CV results reveal that the trends of the optical and electrochemical bandgaps of the polymers were similar, and the lower electronegativity of N over the F atom and the relatively high coplanar backbone are the reasons behind the lower bandgap of **P2-2N**. Thus, by replacing N with F substituents, the HOMO energy levels of the corresponding polymers

are predicted to be further reduced, which is expected to enhance the V_{oc} in the corresponding solar cells. Meanwhile, both these polymers showed complementary absorption and good energy alignment with the non-fullerene acceptor **IT-4F** (HOMO/LUMO = −5.68/−4.15 eV) with a small HOMO energy offset (ΔE_{HOMO} = 0.1 eV < 0.3 eV). Such features proved beneficial for overall charge transport as reported in many recent highly efficient NF-OSCs (Fig. 3(d)).[14,45,55,56]

As shown in Fig. 3(e) and (f), the X-ray diffraction (XRD) technique was utilized to gain information about the packing and molecular orientation properties of pristine **P1-2F** and **P2-2N** polymers. It can be seen from the XRD images that both the polymers had a distinct (100) lamellar stacking peak with 2θ at ~4.7–4.75 $Å^{-1}$ and a (010) π–π stacking peak only in the out-of-plane (OOP) direction. The results manifest that both polymers exhibit a "face-on" packing tendency, which is helpful for vertical charge transport in OSCs.[22,57,58] By fitting the "q" values of the (010) and (100) peaks, the corresponding π–π stacking and lamellar stacking distances were found to be 3.18 Å and 18.78 Å (for **P1-2F**) and 3.12 Å and 18.58 Å (for **P2-2N**), respectively. Furthermore, the coherence length (CCL) estimated using Scherrer's equation (L_C = 2π/FWHM) for the (100) and (010) peaks were found to be 18.41 Å and 3.22 Å for **P1-2F**, and 19.03 Å and 3.73 Å for **P2-2N**, respectively.[59] The shortest lamellar and π–π stacking distances along with relatively larger CCL_{010} and CCL_{100} indicate that **P2-2N** has higher crystallinity among the two polymers. These results clearly show that introducing a pyrazine core in the molecular design is a practical approach for realizing higher crystallinity *via* stronger cofacial π–π stacking compared to the insertion of a fluorinated phenylene core, which is consistent with the high coplanarity observed for the P2-N polymer in the DFT study.

To understand the effect of these structural modifications on the photovoltaic performance of the polymer donors, solar cell devices with the inverted configuration of ITO/ZnO/active layer/MoO_3/Ag were fabricated, and the exact device fabrication conditions are provided in the ESI.† Initially, the donor–acceptor (D–A) blend ratio, the thickness of the active layer and the concentration of different solvent additives were optimized to get the best results (Fig. S10–S13 and Tables S1–S4, ESI†). It was found that the optimized devices of both polymers with similar processing conditions, *i.e.*, polymer : **IT-4F** blend ratio of 1 : 1.1, 0.5% 1,8-diiodooctane (DIO) as the solvent additive and thermal annealing of the active layer at 140 °C for 10 min, yielded the best performance. Fig. 4 illustrates the optimized current density–voltage (*J*–*V*) curves and EQE profiles of the best devices, while detailed photovoltaic parameters are summarized in Table 2. The best **P1-2F:IT-4F**-based devices showed a maximum PCE of 8.1% with the corresponding photovoltaic parameters: a V_{oc} of 0.858 V, a J_{sc} of 17.9 mA cm^{-2}, and a fill factor (FF) of 51.6%, whereas **P2-2N:IT-4F**-based devices showed an increased V_{oc} of 0.878 V, a higher J_{sc} of 18.4 mA cm^{-2}, and a FF of 58.6%, providing a remarkable PCE of 9.5%. To understand the variation in the J_{sc} trend, the absorption coefficients of the optimal blend films were estimated (Fig. 4(b)). Notably, the slightly higher J_{sc} of **P2-2N:IT-4F** blend films originates from its

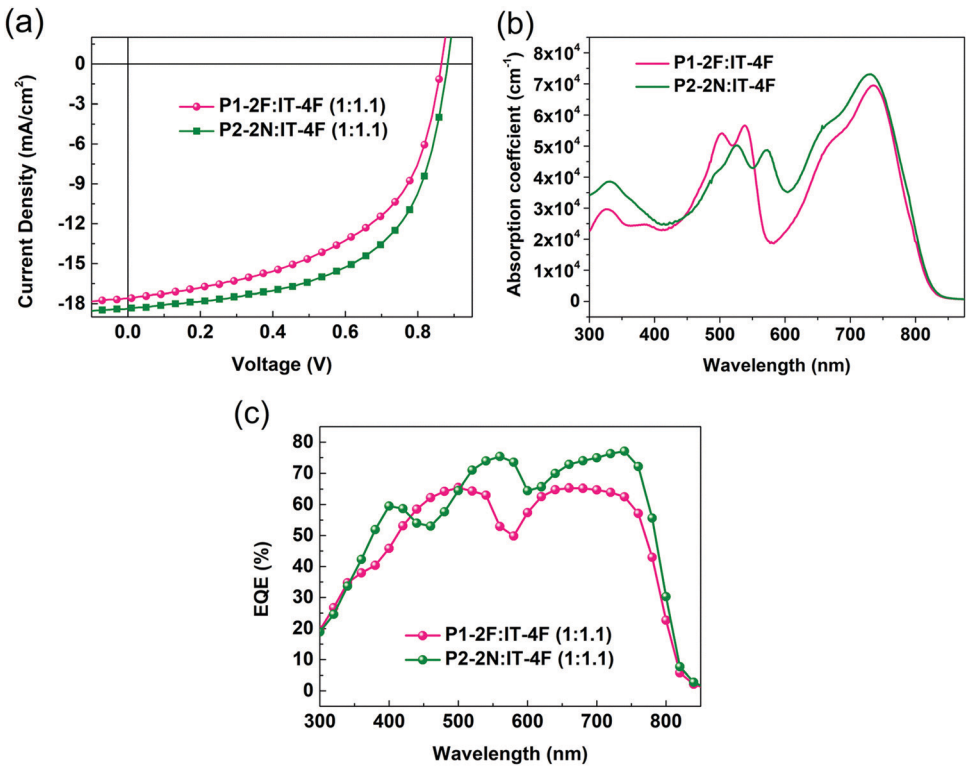

Fig. 4 (a) The *J*–*V* characteristics, (b) absorption coefficients and (c) corresponding EQE spectra of the optimal devices based on **P1-2F**:**IT-4F** and **P2-2N**:**IT-4F**.

Table 2 Photovoltaic performance of different polymer : **IT-4F** (1 : 1.1) solar cell devices processed in CB with 0.5 vol% DIO and thermal annealing at 140 °C for 10 min under AM 1.5G illumination at 100 mW cm^{-2}

Polymer	V_{oc}[a] [V]	J_{sc}[a] [mA cm^{-2}]	FF[a] [%]	E_g^{onset}[b] (eV)	E_{loss}[c] [eV]	PCE[a] [%]	μ_h[d] [cm^2 V^{-1} s^{-1}]	μ_e[e] [cm^2 V^{-1} s^{-1}]	μ_e/μ_h
P1-2F	0.858 (0.856 ± 0.002)	17.6 (17.3 ± 0.4)	53.5 (52.50 ± 1.0)	1.51	0.65	8.1 (8.0)	6.29×10^{-5}	5.47×10^{-4}	8.69
P2-2N	0.878 (0.875 ± 0.003)	18.4 (18.06 ± 0.34)	58.6 (58.16 ± 0.44)	1.49	0.61	9.5 (9.23)	4.10×10^{-4}	6.68×10^{-4}	1.62

Device architecture: ITO/ZnO/active layer/MoO_3/Ag. [a] The average values in parentheses were obtained from 8–10 independent devices. [b] E_g^{onset} is the optical gap of the main light absorber, which is calculated from the EQE spectrum. [c] $E_{loss} = E_g^{onset} - qV_{oc}$, where q is the elementary charge.[62] [d] The configuration of the hole-only device was ITO/PEDOT:PSS/active layer/MoO_3/Ag. [e] The electron-only device had the configuration of ITO/ZnO/active-layer/PDINN/Ag.

much red-shifted absorption of **P2-2N** and well-complimentary absorption profiles of the blend components, which lead to a higher absorption coefficient along 550–750 nm. Besides, they also demonstrated a higher V_{oc} despite a slightly higher HOMO energy compared to **P1-2F** (−5.53 *vs.* −5.57 eV) and a significantly higher FF. As reported previously, in addition to the difference between the HOMO (D) and LUMO (A), the V_{oc} in OSCs is affected by several other factors such as D–A interfaces, charge-transfer states, differences in the intermixing of polymer:acceptor phases, morphology, *etc.*[60,61] Thus, these factors comprehensively acted in **P1-2F**-based devices, which was supported by the PL data, charge carrier mobilities and morphology analysis (discussed below).

To understand the origin of the higher J_{sc} of the **P2-2N:IT-4F**-based devices, the EQE spectra of the optimal devices were compared with the corresponding absorption profiles of the blend films (Fig. 4(b) and (c)). It is evident that the EQE profiles of both the blends nearly imitated the absorption profiles of the optimal blend films, and in addition to a higher photoresponse along the 500–800 nm region, the **P2-2N:IT-4F** blend also demonstrated a maximum EQE (EQE_{max}) of ~80% due to a higher absorption coefficient. Conversely, the **P1-2F:IT-4F** counterpart displayed a lower EQE with an EQE_{max} of ~65%, suggesting that the photocurrent generation in the corresponding solar cells is less efficient than for the **P2-2N:IT-4F** counterpart. These differences mainly arise from the uncomplimentary absorption profiles of the blend components of the **P1-2F:IT-4F** film, leaving behind a valley region around 575 nm. Meanwhile, the J_{sc} values calculated from the EQE profiles matched the J_{sc} values from the *J*–*V* curves within a 5% error. The device energy losses (E_{loss}) are estimated from the equation: $E_{loss} = E_g - qV_{oc}$, where E_g^{onset} was obtained from the EQE spectrum (Table 2).[62] Notably, the E_{loss} of the **P2-2N**-based

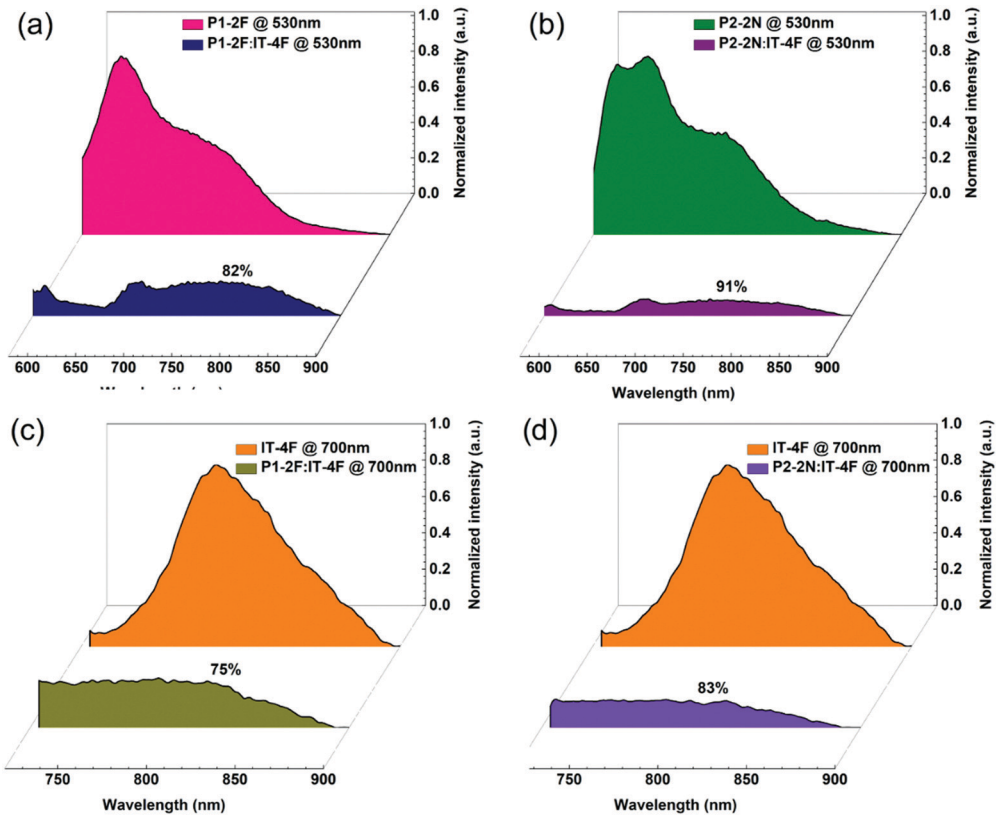

Fig. 5 The PL spectra of pristine (a) **P1-2F** and (b) **P2-2N** (both films excited at 530 nm), (c) and (d) **IT-4F** (excited at 700 nm), and (a) and (c) optimal **P1-2F**:**IT-4F** and (b) and (d) **P2-2N**-based blend films (excited at 530 and 700 nm, respectively).

device was 0.61 eV, which was smaller than that of the **P1-2F** counterpart (0.65 eV).

Next, the difference in the charge dissociation in these blends was estimated using the photoluminescence (PL) quenching method. Firstly, to analyze the extent of photoinduced electron transfer, both the polymers and blends were excited at 530 nm and the corresponding PL emission spectra were recorded (Fig. 5(a) and (b)). Evidently, **P2-2N:IT-4F** displayed better quenching than **P1-2F:IT-4F** (82% *vs.* 91%), suggesting that it has superior photoinduced electron transfer. Likewise, the PL emission spectra of blends and pristine **IT-4F** were obtained by exciting at 700 nm to evaluate the hole transfer efficiency (Fig. 5(c) and (d)). Here also, **P2-2N** outperforms **P1-2F** with superior PL quenching efficiencies of 83% and 75%, respectively. Thus, the higher exciton dissociation efficiency of the **P2-2N**-based blend is one of the factors accountable for the higher J_{sc} in the related devices.

As charge carrier mobility is also a critical factor that affects the J_{sc} and FF variation in the devices, the hole and electron mobilities of the optimal **P1-2F** and **P2-2N** blend films were estimated using the space charge limited current (SCLC) method. The resulting dark *J–V* characteristics and summary of the corresponding devices are presented in Fig. S14 (ESI†) and Table 2. In addition to a significantly higher hole mobility (μ_h) and electron mobility (μ_e) of 4.1×10^{-4} and 6.68×10^{-4} $cm^2\ V^{-1}\ s^{-1}$, respectively, compared to the **P1-2F**-based blend ($\mu_h = 6.29\times 10^{-5}$ and $\mu_e = 5.47 \times 10^{-4}$ $cm^2\ V^{-1}\ s^{-1}$, $\mu_e/\mu_h = 8.69$), the optimal **P2-2N**-based blend film also demonstrated a superior balance between μ_h and μ_e of 1.62. It is well known that high μ_h values aid in efficient charge transport in OSCs *via* suppression of the bimolecular and Shockley–Read–Hall recombination. Moreover, a superior balance between μ_e and μ_h will further assist in minimizing the built-in space charges, thus subsequently helping in boosting the PCE by increasing the J_{sc} and FF.[63]

Then film microstructure and molecular packing within the optimized blend films were studied using atomic force microscopy (AFM), transmission electron microscopy (TEM) and XRD to further correlate the variation in the V_{oc} and FF in the optimized devices. As shown in the AFM images (Fig. 6(a)–(c)), the **P1-2F**-based film demonstrated a distinct phase-separated morphology with larger domain sizes of **P1-2F** and **IT-4F** phases (>100 nm) along with a relatively large root-mean-square (RMS) roughness of 7.53 nm. Such a morphology proved to cause charge trapping, limiting the charge dissociation and transport by increasing the degree of charge recombination, which, in turn, leads to a poor V_{oc} and FF and a low efficiency.[64] In contrast, **P2-2N**-based blends films had a relatively smooth and uniform morphology with a smaller domain size (<40 nm) along with an RMS roughness of 1.85 nm (Fig. 6(e)–(h)). The TEM analysis further reveals that the **P2-2N:IT-4F** film has better miscibility and favorable well-interconnected domains with appropriate phase separation than the **P1-2F**-blend film, which is beneficial for exciton dissociation and charge collection by increasing the D–A interfacial areas (Fig. 6(d) and (h)). Thus, the superior nanoscale morphology of the **P2-2N:IT-4F** film serves as an effective pathway for overall charge dissociation and collection by forming good contact with the electrodes, consistent with the more efficient exciton dissociation and higher FF displayed by these blends. Lastly, the XRD images of both blends reveal apparent changes in (100) and (010) scattering relative to the pristine polymer films, suggesting that the molecular packing and orientation of both polymers were affected by the mixing of the **IT-4F** acceptor (Fig. S15, ESI†). Interestingly, the **P1-2F:IT-4F**-based blend showed higher molecular ordering with shorter lamellar and π–π stacking distances compared to **P2-2N**-blends (20.53 and 3.18 Å *vs.* 21.63 and 3.19 Å, respectively) and retained face-on molecular orientation as summarized in Fig. S10 (ESI†). These results imply the aggregation of **P1-2F** phases in devices, which may affect the overall charge transport reducing the D–A interfaces and leading to charge transfer pathways.[65] Thus, the poor morphology of the **P1-2F:IT-4F**-based film is the main reason behind its lower charge mobility,

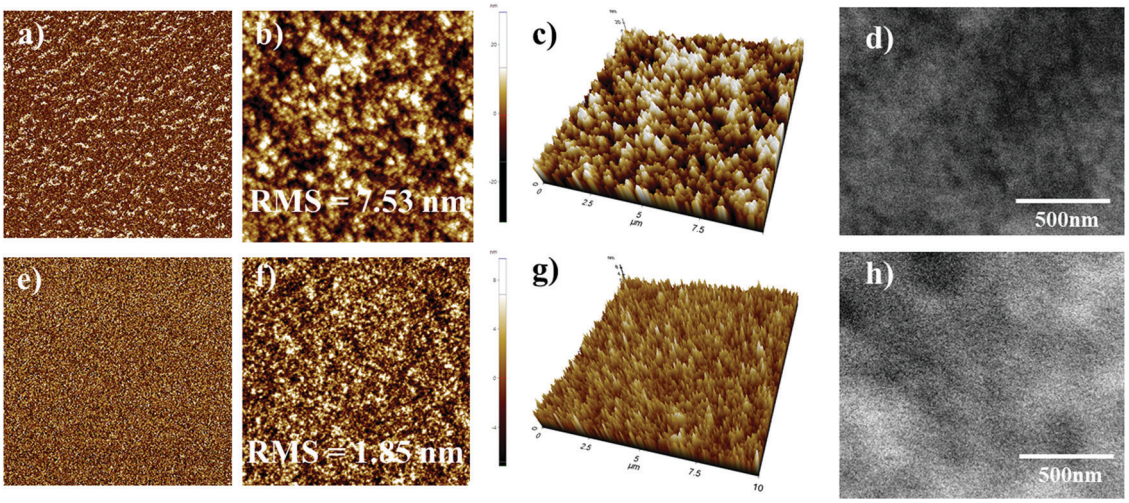

Fig. 6 Phase, height, three-dimensional topography of AFM images and TEM images of the (a)–(d) **P1-2F**:**IT-4F** and (e)–(h) **P2-2N**:**IT-4F** blend films, respectively.

poor exciton harvesting and lower PCE. However, **P2-2N:IT-4F** remarkably maintains face-on molecular orientation with good miscibility and intermixing of the **IT-4F** phases, as indicated by the slight increase of lamellar spacing and *d*-spacing distance to pristine **P2-2N** films. Therefore, favorable molecular packing with the retention of ''face-on'' molecular ordering of the **P2-2N:IT-4F** film assisted efficient charge transport in OSCs and helped to realize high J_{sc}, FF, and enhanced PCE values.

3. Conclusion

In conclusion, we systematically elucidated the synergistic effect of the insertion of fluorine and nitrogen substituents on the properties and photovoltaic performance of polymer donors by synthesizing two new polymers, **P1-2F** and **P2-2N**. Owing to the higher electronegativity of F compared to N atoms and F···S and F···H noncovalent intermolecular locks, **P1-2F** displayed good coplanarity and deeper HOMO and LUMO energy levels than **P2-2N**. Still, the inferior phase-separated morphology mixing with **IT-4F** led to a lower charge carrier mobility and photovoltaic performance of 8.1% in **P1-2F**-based devices. Interestingly, molecular planarity was further improved in **P2-2N** due to the superior positioning of the N atom in conjugation with the benzene core as releveled by DFT, which subsequently favored enhanced optical absorption, compact molecular packing, a longer coherence length, a high charge carrier mobility and favorable morphology. As a result, **P2-2N:IT-4F** based devices produced the highest PCE of 9.5% with an overall improvement in all device parameters, *i.e.*, a V_{oc} of 0.878 V, a higher J_{sc} of 18.4 mA cm^{-2}, a FF of 58.6% and a low E_{loss} of 0.61 eV. Overall, these results illuminate the distinct merits and drawbacks of F···S and N···S NCLs on the molecular planarity, energy levels, molecular packing, and crystallinity and consequently provide valuable guidelines to choose between two substituents to develop high PCE low-cost polymer donors.

Conflicts of interest

There are no conflicts to declare.

Acknowledgements

This work was supported by the Korea Institute of Energy Technology Evaluation and Planning (KETEP) and the Ministry of Trade, Industry & Energy (MOTIE) of the Republic of Korea (No. 20194010201790) and the National Research Foundation of Korea (NRF) (No. 2020R1A2C2010916).

References

1 L. Lu, T. Zheng, Q. Wu, A. M. Schneider, D. Zhao and L. Yu, Recent advances in bulk heterojunction polymer solar cells, *Chem. Rev.*, 2015, **115**(23), 12666–12731.
2 Y. Ma, Z. Kang and Q. Zheng, Recent advances in wide bandgap semiconducting polymers for polymer solar cells, *J. Mater. Chem. A*, 2017, **5**(5), 1860–1872.
3 S. Berny, N. Blouin, A. Distler, H.-J. Egelhaaf, M. Krompiec, A. Lohr, O. R. Lozman, G. E. Morse, L. Nanson, A. Pron, T. Sauermann, N. Seidler, S. Tierney, P. Tiwana, M. Wagner and H. Wilson, Solar trees: First large-scale demonstration of fully solution coated, semitransparent, flexible organic photovoltaic modules, *Adv. Sci.*, 2016, **3**(5), 1500342.
4 Y. Li, G. Xu, C. Cui and Y. Li, Flexible and semitransparent organic solar cells, *Adv. Energy Mater.*, 2018, **8**(7), 1701791.
5 G. P. Kini, S. J. Jeon and D. K. Moon, Design principles and synergistic effects of chlorination on a conjugated backbone for efficient organic photovoltaics: A critical Review, *Adv. Mater.*, 2020, **32**(11), 1906175.
6 G. P. Kini, S. J. Jeon and D. K. Moon, Latest progress on photoabsorbent materials for multifunctional semitransparent organic solar cells, *Adv. Funct. Mater.*, 2021, **31**(15), 2007931.
7 G. P. Kini, Y. W. Han, S. J. Jeon, E. J. Lee, Y. J. Lee, M. Goh and D. K. Moon, Tailoring microstructure and morphology *via* sequential fluorination to enhance the photovoltaic performance of low-cost polymer donors for organic solar cells, *Macromol. Rapid Commun.*, 2022, 2200070.
8 S. Dey, Recent progress in molecular design of fused ring electron acceptors for organic solar cells, *Small*, 2019, **15**(21), 1900134.
9 G. Zhang, J. Zhao, P. C.-Y. Chow, K. Jiang, J. Zhang, Z. Zhu, J. Zhang, F. Huang and H. Yan, Nonfullerene acceptor molecules for bulk heterojunction organic solar cells, *Chem. Rev.*, 2018, **118**(7), 3447–3507.
10 C. Li, H. Fu, T. Xia and Y. Sun, Asymmetric nonfullerene small molecule acceptors for organic solar cells, *Adv. Energy Mater.*, 2019, **9**(25), 1900999.
11 H. Wang, J. Cao, J. Yu, Z. Zhang, R. Geng, L. Yang and W. Tang, Molecular engineering of central fused-ring cores of non-fullerene acceptors for high-efficiency organic solar cells, *J. Mater. Chem. A*, 2019, **7**(9), 4313–4333.
12 S. Li, C.-Z. Li, M. Shi and H. Chen, New phase for organic solar cell research: Emergence of Y-series electron acceptors and their perspectives, *ACS Energy Lett.*, 2020, **5**(5), 1554–1567.
13 Z.-Q. Jiang, T.-T. Wang, F.-P. Wu, J.-D. Lin and L.-S. Liao, Recent advances in electron acceptors with ladder-type backbone for organic solar cells, *J. Mater. Chem. A*, 2018, **6**(36), 17256–17287.
14 Y. Cui, H. Yao, J. Zhang, T. Zhang, Y. Wang, L. Hong, K. Xian, B. Xu, S. Zhang, J. Peng, Z. Wei, F. Gao and J. Hou, Over 16% efficiency organic photovoltaic cells enabled by a chlorinated acceptor with increased open-circuit voltages, *Nat. Commun.*, 2019, **10**(1), 2515.
15 Q. Liu, Y. Jiang, K. Jin, J. Qin, J. Xu, W. Li, J. Xiong, J. Liu, Z. Xiao, K. Sun, S. Yang, X. Zhang and L. Ding, 18% Efficiency organic solar cells, *Sci. Bull.*, 2020, **65**(4), 272–275.

16 X. Xu, K. Feng, Z. Bi, W. Ma, G. Zhang and Q. Peng, Single-junction polymer solar cells with 16.35% efficiency enabled by a platinum(II) complexation strategy, *Adv. Mater.*, 2019, **31**(29), 1901872.

17 T. Yan, W. Song, J. Huang, R. Peng, L. Huang and Z. Ge, 16.67% rigid and 14.06% flexible organic solar cells enabled by ternary heterojunction strategy, *Adv. Mater.*, 2019, **31**, 1902210.

18 L. Zhan, S. Li, T.-K. Lau, Y. Cui, X. Lu, M. Shi, C.-Z. Li, H. Li, J. Hou and H. Chen, Over 17% efficiency ternary organic solar cells enabled by two non-fullerene acceptors working in an alloy-like model, *Energy Environ. Sci.*, 2020, **13**(2), 635–645.

19 W. Zhang, J. Huang, J. Xu, M. Han, D. Su, N. Wu, C. Zhang, A. Xu and C. Zhan, Phthalimide polymer donor guests enable over 17% efficient organic solar cells *via* parallel-like ternary and quaternary strategies, *Adv. Energy Mater.*, 2020, **10**(32), 2001436.

20 Y. Cui, H. Yao, J. Zhang, K. Xian, T. Zhang, L. Hong, Y. Wang, Y. Xu, K. Ma, C. An, C. He, Z. Wei, F. Gao and J. Hou, Single-junction organic photovoltaic cells with approaching 18% efficiency, *Adv. Mater.*, 2020, **32**(19), 1908205.

21 Q. An, J. Wang, W. Gao, X. Ma, Z. Hu, J. Gao, C. Xu, M. Hao, X. Zhang, C. Yang and F. Zhang, Alloy-like ternary polymer solar cells with over 17.2% efficiency, *Sci. Bull.*, 2020, **65**(7), 538–545.

22 S. Li, L. Ye, W. Zhao, H. Yan, B. Yang, D. Liu, W. Li, H. Ade, J. Hou and A. Wide, Band gap polymer with a deep highest occupied molecular orbital level enables 14.2% efficiency in polymer solar cells, *J. Am. Chem. Soc.*, 2018, **140**(23), 7159–7167.

23 J. Wu, Q. Fan, M. Xiong, Q. Wang, K. Chen, H. Liu, M. Gao, L. Ye, X. Guo, J. Fang, Q. Guo, W. Su, Z. Ma, Z. Tang, E. Wang, H. Ade and M. Zhang, Carboxylate substituted pyrazine: A simple and low-cost building block for novel wide bandgap polymer donor enables 15.3% efficiency in organic solar cells, *Nano Energy*, 2021, **82**, 105679.

24 F. Zhao, J. Zhou, D. He, C.-R. Wang and Y. Lin, Low-cost materials for organic solar cells, *J. Mater. Chem. C*, 2021, **9**, 15395–15406.

25 X. Yuan, Y. Zhao, T. Zhan, J. Oh, J. Zhou, J. Li, X. Wang, Z. Wang, S. Pang, P. Cai, C. Yang, Z. He, Z. Xie, C. Duan, F. Huang and Y. Cao, A donor polymer based on 3-cyanothiophene with superior batch-to-batch reproducibility for high-efficiency organic solar cells, *Energy Environ. Sci.*, 2021, **14**(10), 5530–5540.

26 T. Wang, J. Qin, Z. Xiao, J. Zhang, Z. Chen, L. Zhang, M. Cheng, Z. Jin, Y. Yuan, W.-Q. Wu, C. Duan, S. Xie, K. Sun, F. Hao and L. Ding, Multiple conformation locks gift polymer donor high efficiency, *Nano Energy*, 2020, **77**, 105161.

27 G. Zhang, H. Ning, H. Chen, Q. Jiang, J. Jiang, P. Han, L. Dang, M. Xu, M. Shao, F. He and Q. Wu, Naphthalenothiophene imide-based polymer exhibiting over 17% efficiency, *Joule*, 2021, **5**(4), 931–944.

28 H. Huang, L. Yang, A. Facchetti and T. J. Marks, Organic and polymeric semiconductors enhanced by noncovalent conformational locks, *Chem. Rev.*, 2017, **117**(15), 10291–10318.

29 S. Yu, A. Peng, S. Zhang and H. Huang, Noncovalent conformational locks in organic semiconductors, *Sci. China: Chem.*, 2018, **61**(11), 1359–1367.

30 N. E. Jackson, B. M. Savoie, K. L. Kohlstedt, M. Olvera de la Cruz, G. C. Schatz, L. X. Chen and M. A. Ratner, Controlling conformations of conjugated polymers and small molecules: The role of nonbonding interactions, *J. Am. Chem. Soc.*, 2013, **135**(28), 10475–10483.

31 S. Shi, Q. Liao, Y. Tang, H. Guo, X. Zhou, Y. Wang, T. Yang, Y. Liang, X. Cheng, F. Liu and X. Guo, Head-to-head linkage containing bithiophene-based polymeric semiconductors for highly efficient polymer solar cells, *Adv. Mater.*, 2016, **28**(45), 9969–9977.

32 B.-S. Lu, Y. Zhang, T.-Y. Hu, Y.-F. Ma, Y.-N. Zhu, D.-W. Liu, Z.-Q. Zhang, E. Wang, W. Ma and H.-L. Zhang, Non-fullerene acceptors based on multiple noncovalent interactions for low cost and air stable organic solar cells, *Org. Electron.*, 2021, **93**, 106132.

33 X. Li, F. Pan, C. Sun, M. Zhang, Z. Wang, J. Du, J. Wang, M. Xiao, L. Xue, Z.-G. Zhang, C. Zhang, F. Liu and Y. Li, Simplified synthetic routes for low cost and high photovoltaic performance n-type organic semiconductor acceptors, *Nat. Commun.*, 2019, **10**(1), 519.

34 S. Li, W. Zhao, J. Zhang, X. Liu, Z. Zheng, C. He, B. Xu, Z. Wei and J. Hou, Influence of covalent and noncovalent backbone rigidification strategies on the aggregation structures of a wide-band-gap polymer for photovoltaic cells, *Chem. Mater.*, 2020, **32**(5), 1993–2003.

35 G. P. Kini, H. S. Park, S. J. Jeon, Y. W. Han and D. K. Moon, A 2,5-difluoro benzene-based low cost and efficient polymer donor for non-fullerene solar cells, *Sol. Energy*, 2020, **207**, 720–728.

36 S. Yu, Y. Chen, L. Yang, P. Ye, J. Wu, J. Yu, S. Zhang, Y. Gao and H. Huang, Significant enhancement of photovoltaic performance through introducing S–N conformational locks, *J. Mater. Chem. A*, 2017, **5**(41), 21674–21678.

37 Z.-P. Yu, Z.-X. Liu, F.-X. Chen, R. Qin, T.-K. Lau, J.-L. Yin, X. Kong, X. Lu, M. Shi, C.-Z. Li and H. Chen, Simple non-fused electron acceptors for efficient and stable organic solar cells, *Nat. Commun.*, 2019, **10**(1), 2152.

38 H. Huang, Q. Guo, S. Feng, C.-e Zhang, Z. Bi, W. Xue, J. Yang, J. Song, C. Li, X. Xu, Z. Tang, W. Ma and Z. Bo, Noncovalently fused-ring electron acceptors with near-infrared absorption for high-performance organic solar cells, *Nat. Commun.*, 2019, **10**(1), 3038.

39 J. Gao, Y. Li, S. Li, X. Xia, X. Lu, M. Shi and H. Chen, Non-fullerene acceptors with nitrogen-containing six-membered heterocycle cores for the applications in organic solar cells, *Sol. Energy Mater. Sol. Cells*, 2021, **225**, 111046.

40 G. P. Kini, J. Y. Choi, S. J. Jeon, I. S. Suh and D. K. Moon, Effects of incorporated pyrazine on the interchain packing and photovoltaic properties of wide-bandgap D–A polymers

for non-fullerene polymer solar cells, *Polym. Chem.*, 2019, **10**(32), 4459–4468.

41 Q. Zhang, M. A. Kelly, N. Bauer and W. You, The Curious case of fluorination of conjugated polymers for solar cells, *Acc. Chem. Res.*, 2017, **50**(9), 2401–2409.

42 N. Leclerc, P. Chávez, O. A. Ibraikulov, T. Heiser and P. Lévêque, Impact of backbone fluorination on π-conjugated polymers in organic photovoltaic devices: A review, *Polymers*, 2016, **8**(1), 11.

43 Q. Fan, U. A. Méndez-Romero, X. Guo, E. Wang, M. Zhang and Y. Li, Fluorinated photovoltaic materials for high-performance organic solar cells, *Chem. – Asian J.*, 2019, **14**(18), 3085–3095.

44 H.-H. Cho, T. E. Kang, K.-H. Kim, H. Kang, H. J. Kim and B. J. Kim, Effect of incorporated nitrogens on the planarity and photovoltaic performance of donor–acceptor copolymers, *Macromolecules*, 2012, **45**(16), 6415–6423.

45 T. Wang, R. Sun, S. Xu, J. Guo, W. Wang, J. Guo, X. Jiao, J. Wang, S. Jia, X. Zhu, Y. Li and J. Min, A wide-bandgap D–A copolymer donor based on a chlorine substituted acceptor unit for high performance polymer solar cells, *J. Mater. Chem. A*, 2019, **7**(23), 14070–14078.

46 A. L. Allred and A. L. Hensley, Electronegativities of nitrogen, phosphorus, arsenic, antimony and bismuth, *J. Inorg. Nucl. Chem.*, 1961, **17**(1), 43–54.

47 M. L. Tang and Z. Bao, Halogenated materials as organic semiconductors, *Chem. Mater.*, 2011, **23**(3), 446–455.

48 Carbon–nitrogen bond. Carbon–nitrogen bond - Wikipedia.

49 W. Zhao, S. Li, H. Yao, S. Zhang, Y. Zhang, B. Yang and J. Hou, Molecular optimization enables over 13% efficiency in organic solar cells, *J. Am. Chem. Soc.*, 2017, **139**(21), 7148–7151.

50 S. S. Batsanov, van der Waals radii of elements, *Inorg. Mater.*, 2001, **37**(9), 871–885.

51 J. Chen, Z. Yan, L. Tang, M. A. Uddin, J. Yu, X. Zhou, K. Yang, Y. Tang, T. J. Shin, H. Y. Woo and X. Guo, 1, 4-di(3-alkoxy-2-thienyl)-2,5-difluorophenylene: A building block enabling high-performance polymer semiconductors with increased open-circuit voltages, *Macromolecules*, 2018, **51**(14), 5352–5363.

52 G. P. Kini, E. J. Lee, S. J. Jeon and D. K. Moon, Understanding the critical role of sequential fluorination of phenylene units on the properties of dicarboxylate bithiophene-based wide-bandgap polymer donors for non-fullerene organic solar cells, *Macromol. Rapid Commun.*, 2021, **42**(9), 2000743.

53 T. Duan, J. Gao, T. Xu, Z. Kan, W. Chen, R. Singh, G. P. Kini, C. Zhong, D. Yu, Z. Xiao, Z. Xiao and S. Lu, Simple organic donors based on halogenated oligothiophenes for all small molecule solar cells with efficiency over 11%, *J. Mater. Chem. A*, 2020, **8**(12), 5843–5847.

54 G. P. Kini, S. R. Suranagi, M. Kumar and R. Singh, A systematic evaluation of triisopropylsilylethynyl-substituted thienyl side chain effects on series of benzo[1,2-*b*:4,5-*b*′]dithiophene based polymer donors and their photovoltaic performances, *Dyes Pigm.*, 2020, **175**, 108083.

55 J. Zhang, Y. Li, H. Hu, G. Zhang, H. Ade and H. Yan, Chlorinated thiophene end groups for highly crystalline alkylated non-fullerene acceptors toward efficient organic solar cells, *Chem. Mater.*, 2019, **31**(17), 6672.

56 Z. Zhang, W. Liu, T. Rehman, H.-X. Ju, J. Mai, X. Lu, M. Shi, J. Zhu, C.-Z. Li and H. Chen, Energy-level modulation of non-fullerene acceptors to achieve high-efficiency polymer solar cells at a diminished energy offset, *J. Mater. Chem. A*, 2017, **5**(20), 9649–9654.

57 J. Yang, M. A. Uddin, Y. Tang, Y. Wang, Y. Wang, H. Su, R. Gao, Z.-K. Chen, J. Dai, H. Y. Woo and X. Guo, Quinoxaline-based wide band gap polymers for efficient nonfullerene organic solar cells with large open-circuit voltages, *ACS Appl. Mater. Interfaces*, 2018, **10**(27), 23235–23246.

58 Y. Wu, H. Yang, Y. Zou, Y. Dong, J. Yuan, C. Cui and Y. Li, A new dialkylthio-substituted naphtho[2,3-*c*]thiophene-4, 9-dione based polymer donor for high-performance polymer solar cells, *Energy Environ. Sci.*, 2019, **12**(2), 675–683.

59 G. Zhang, X. Xu, Z. Bi, W. Ma, D. Tang, Y. Li and Q. Peng, Fluorinated and alkylthiolated polymeric donors enable both efficient fullerene and nonfullerene polymer solar cells, *Adv. Funct. Mater.*, 2018, **28**(10), 1706404.

60 Y. Li, H. Meng, T. Liu, Y. Xiao, Z. Tang, B. Pang, Y. Li, Y. Xiang, G. Zhang, X. Lu, G. Yu, H. Yan, C. Zhan, J. Huang and J. Yao, 8.78% efficient all-polymer solar cells enabled by polymer acceptors based on a b ← n embedded electron-deficient unit, *Adv. Mater.*, 2019, **31**(44), 1904585.

61 X. Zhao, T. Wang, W. Wang, R. Sun, Q. Wu, H. Shen, J. Xia, Y. Wang, M. Zhang and J. Min, Polymerized small-molecule acceptors based on vinylene as π-bridge for efficient all-polymer solar cells, *Polymer*, 2021, **230**, 124104.

62 Y. Tang, H. Sun, Z. Wu, Y. Zhang, G. Zhang, M. Su, X. Zhou, X. Wu, W. Sun, X. Zhang, B. Liu, W. Chen, Q. Liao, H. Y. Woo, X. Guo and A. New, Wide bandgap donor polymer for efficient nonfullerene organic solar cells with a large open-circuit voltage, *Adv. Sci.*, 2019, **6**(21), 1901773.

63 S. H. Park, G. E. Park, S. Choi, Y. U. Kim, S. Y. Park, C. G. Park, M. J. Cho and D. H. Choi, Effect of a methyl thiophene-3-carboxylate bridge in an indacenodithiophene-based acceptor–donor–acceptor-type molecule on the performance of non-fullerene polymer solar cells, *J. Mater. Chem. C*, 2018, **6**(28), 7549–7556.

64 Y. Wu, C. An, L. Shi, L. Yang, Y. Qin, N. Liang, C. He, Z. Wang and J. Hou, The crucial role of chlorinated thiophene orientation in conjugated polymers for photovoltaic devices, *Angew. Chem., Int. Ed.*, 2018, **57**(39), 12911–12915.

65 G. P. Kini, S. Oh, Z. Abbas, S. Rasool, M. Jahandar, C. E. Song, S. K. Lee, W. S. Shin, W.-W. So and J.-C. Lee, Effects on photovoltaic performance of dialkyloxy-benzothiadiazole copolymers by varying the thienoacene donor, *ACS Appl. Mater. Interfaces*, 2017, **9**(14), 12617–12628.